The Astrophysical Journal Supplement Series, 147:421–435, 2003 August

DIELECTRONIC RECOMBINATION OF Fe XXI AND Fe XXII VIA $N = 2 \rightarrow N' = 2$ CORE EXCITATIONS

D. W. Savin and S. M. Kahn
Columbia Astrophysics Laboratory and Department of Physics, Columbia University, New York, NY 10027;
savin@astro.columbia.edu

G. Gwinner, M. Grieser, R. Repnow, G. Saathoff, D. Schwalm, and A. Wolf
Max-Planck-Institut für Kernphysik, D-69117 Heidelberg, Germany

A. Müller and S. Schippers
Institut für Kernphysik, Strahlenzentrum, Justus-Liebig-Universität, D-35392 Giessen, Germany

P. A. Závodszky
National Superconducting Cyclotron Laboratory, Michigan State University, East Lansing, MI 48824

M. H. Chen
Lawrence Livermore National Laboratory, Livermore, CA 94550

T. W. Gorczyca and O. Zatsarinny
Department of Physics, Western Michigan University, Kalamazoo, MI 49008

and

M. F. Gu[1]
Center for Space Research, Massachusetts Institute of Technology, Cambridge, MA 02139
Received 2003 March 10; accepted 2003 April 2

ABSTRACT

We have measured dielectronic recombination (DR) resonance strengths and energies for carbon-like Fe XXI forming Fe XX and for boron-like Fe XXII forming Fe XXI via $N = 2 \rightarrow N' = 2$ core excitations. All measurements were carried out using the heavy-ion Test Storage Ring at the Max-Planck-Institute for Nuclear Physics in Heidelberg, Germany. We have also calculated these resonance strengths and energies using three independent, state-of-the-art perturbative techniques: a multiconfiguration Breit-Pauli (MCBP) method using the code AUTOSTRUCTURE, a multiconfiguration Dirac-Fock (MCDF) method, and a relativistic configuration interaction method using the Flexible Atomic Code (FAC). Overall, reasonable agreement is found between our experimental results and our theoretical calculations. The most notable discrepancies tend to occur for relative collision energies $\lesssim 3$ eV. We have used our measured $2 \rightarrow 2$ results to produce Maxwellian-averaged rate coefficients for Fe XXI and Fe XXII. Our experimentally derived rate coefficients are estimated to be accurate to better than $\approx$20% both for Fe XXI at $k_B T_e > 0.5$ eV and for Fe XXII at $k_B T_e > 0.001$ eV. For these results, we provide fits that are accurate to better than 0.5% for Fe XXI at 0.001 eV $\leq k_B T_e \leq 10,000$ eV and for Fe XXII at 0.02 eV $\lesssim k_B T_e \leq 10,000$ eV. Our fitted rate coefficients are suitable for ionization balance calculations involving Fe XXI and Fe XXII in photoionized plasmas. Previous published Burgess formula and LS-coupling calculations are in poor agreement with our experimentally derived rate coefficients. None of these published calculations reliably reproduce the magnitude or temperature dependence of our experimental results. Our previously published Fe XXI MCDF results are in good agreement with our experimental results for $k_B T_e \gtrsim 0.07$ eV. For both ions in this temperature range our new MCBP, MCDF, and FAC results are in excellent agreement with our experimentally derived rate coefficient.

Subject headings: atomic data — atomic processes — methods: laboratory

1. INTRODUCTION

For most ions in X-ray photoionized plasmas, low-temperature dielectronic recombination (DR) is the dominant electron-ion recombination mechanism (Ferland et al. 1998). Such plasmas form in the media surrounding cataclysmic variables, active galactic nuclei, and X-ray binaries (Kallman & Bautista 2001). Interpreting and modeling spectra from these sources requires reliable low-temperature DR data. Particularly important are the DR rate coefficients for the iron L-shell ions (Fe XVIII–Fe XXIV). These ions are predicted to play an important role in determining the thermal structure and line emission from X-ray photoionized plasmas (Hess, Kahn, & Paerels 1997; Savin et al. 1999, 2000; Gu 2003a).

DR is a two-step recombination process that begins when a free electron approaches an ion, collisionally excites a bound electron of the ion, and is simultaneously captured. The electron excitation can be labeled $Nl_j \rightarrow N'l'_{j'}$, where N is the principal quantum number of the core electron, l is its orbital angular momentum, and j is its total angular momentum. This intermediate state, formed by the simultaneous excitation and capture, may autoionize. The DR process is complete when the intermediate state emits a photon which reduces the total energy of the recombined ion to below its ionization limit. Conservation of energy requires that for DR to go forward $E_k = \Delta E - E_b$. Here E_k is the kinetic energy of the incident electron, ΔE is the excitation energy of the initially bound electron, and E_b is the binding

[1] *Chandra* Fellow.

energy released when the incident electron is captured onto the excited ion. Because ΔE and E_b are quantized, DR is a resonant process. DR via $N = 2 \rightarrow N' = 2$ core excitations (i.e., $2 \rightarrow 2$ DR) generally dominates the DR process for iron L-shell ions in photoionized plasmas (Savin et al. 1997, 2000, 2002a, 2002b).

To address the need for accurate low-temperature DR rate coefficients of iron L-shell ions, we have carried out a series of measurements for DR via $2 \rightarrow 2$ core excitations. The data were collected using the heavy-ion Test Storage Ring (TSR) located at the Max-Planck-Institute for Nuclear Physics in Heidelberg, Germany (Müller & Wolf 1997). Recently, we have completed measurements of $2 \rightarrow 2$ DR for Fe XVIII–Fe XXIV. We use the convention here of identifying the recombination process by the initial charge state of the recombining ion. Results have been published for Fe XVIII (Savin et al. 1997, 1999), Fe XIX (Savin et al. 1999, 2002a), and Fe XX (Savin et al. 2002b). In this paper we present results for Fe XXI and Fe XXII. Results for Fe XXIII and Fe XXIV will be presented in future publications.

DR via $2 \rightarrow 2$ core excitations can proceed via a number of different intermediate autoionizing states. DR occurs when these autoionizing states radiatively stabilize to a bound configuration of the recombined ion. Carbon-like Fe XXI can undergo DR by $2 \rightarrow 2$ core excitations via the following resonances:

$$\mathrm{Fe}^{20+}(2s^2 2p^2[^3P_0]) + e^- \rightarrow \begin{cases} \mathrm{Fe}^{19+}(2s^2 2p^2[^3P_{1,2};\ ^1D_2;\ ^1S_0]nl)\ ; \\ \mathrm{Fe}^{19+}(2s2p^3[^5S^o_2;\ ^3D^o_{1,2,3};\ ^3P^o_{0,1,2};\ ^3S^o_1;\ ^1D^o_2;\ ^1P^o_1]nl)\ ; \\ \mathrm{Fe}^{19+}(2p^4[^3P_{2,0,1};\ ^1D_2;\ ^1S_0]nl)\ . \end{cases} \quad (1)$$

In our measurements we were able to measure DR resonances for electron-ion collision energies between 0 and ≈135 eV. Boron-like Fe XXII can undergo DR by $2 \rightarrow 2$ core excitations via the following resonances:

$$\mathrm{Fe}^{21+}(2s^2 2p[^2P^o_{1/2}]) + e^- \rightarrow \begin{cases} \mathrm{Fe}^{20+}(2s^2 2p[^2P^o_{3/2}]nl)\ ; \\ \mathrm{Fe}^{20+}(2s2p^2[^4P_{1/2,3/2,5/2};\ ^2D_{3/2,5/2};\ ^2P_{1/2\ 3/2};\ ^2S_{1/2}]nl)\ ; \\ \mathrm{Fe}^{20+}(2p^3[^4S^o_{3/2};\ ^2D^o_{3/2,5/2};\ ^2P^o_{1/2,3/2}]nl)\ . \end{cases} \quad (2)$$

We were able to measure DR resonances for electron-ion collision energies between 0 and ≈123 eV. The excitation energies ΔE for all Fe XXI and Fe XXII levels in the $n = 2$ shell are listed, relative to the ground state, in Tables 1 and 2, respectively.

The strength of a DR resonance is given by the integral of the resonance cross section over energy. In the isolated resonance approximation, the integrated strength of a particular DR resonance S_d can be approximated as (Kilgus et al. 1992)

$$S_d = \frac{h\mathscr{R}}{E_d}\pi a_0^2 \frac{g_d}{2g_i} \frac{A_a(d \rightarrow i)\sum_f A_r(d \rightarrow f)}{\sum_\kappa A_a(d \rightarrow \kappa) + \sum_{f'} A_r(d \rightarrow f')}\ . \quad (3)$$

Here h is the Planck constant; $\mathscr{R}$ is the Rydberg energy constant; E_d is the energy of resonance d; a_0 is the Bohr radius; g_d and g_i are the statistical weights of d and of the initial ion, respectively; A_a and A_r are the autoionization and radiative decay rates, respectively; $\sum_f$ is over all states stable against autoionization; $\sum_{f'}$ is over all states energetically below d; both $\sum_f$ and $\sum_{f'}$ may include cascades through lower lying autoionizing states and ultimately to bound states; and $\sum_\kappa$ is over all states attainable by autoionization of d.

This paper is organized as follows: In § 2 we briefly discuss the experimental technique. Section 3 presents our experimental results. Existing and new theoretical calculations are discussed in § 4. In § 5 we discuss the comparison between theory and our experimental results. Conclusions are given in § 6.

TABLE 1
EXPERIMENTAL AND THEORETICAL Fe XXI TARGET ENERGIES (RELATIVE TO THE GROUND STATE) IN eV

Level	Experiment[a]	MCBP	MCDF	FAC
$1s^2 2s^2 2p^2(^3P_0)$	0.0	0.0	0.0	0.0
$1s^2 2s^2 2p^2(^3P_1)$	9.156	8.957	9.147	9.105
$1s^2 2s^2 2p^2(^3P_2)$	14.550	14.682	14.626	14.573
$1s^2 2s^2 2p^2(^1D_2)$	30.321	30.340	30.578	30.526
$1s^2 2s^2 2p^2(^1S_0)$	46.10	45.283	46.269	46.222
$1s^2 2s2p^3(^5S^o_2)$	60.374	58.361	58.796	59.176
$1s^2 2s2p^3(^3D^o_1)$	96.308	95.832	96.119	96.549
$1s^2 2s2p^3(^3D^o_2)$	96.379	95.937	96.138	96.579
$1s^2 2s2p^3(^3D^o_3)$	99.674	99.586	99.360	99.794
$1s^2 2s2p^3(^3P^o_0)$	113.61	112.82	113.77	113.95
$1s^2 2s2p^3(^3P^o_1)$	114.67	114.09	114.60	115.01
$1s^2 2s2p^3(^3P^o_2)$	116.83	116.40	116.77	117.14
$1s^2 2s2p^3(^3S^o_1)$	135.83	136.39	137.28	136.95
$1s^2 2s2p^3(^1D^o_2)$	139.70	140.68	140.95	141.00
$1s^2 2s2p^3(^1P^o_1)$	156.3	156.95	157.73	157.68
$1s^2 2p^4(^3P_2)$	204.11	204.46	204.36	205.08
$1s^2 2p^4(^3P_0)$	215.19	215.39	215.56	216.22
$1s^2 2p^4(^3P_1)$	215.79	215.84	215.98	216.68
$1s^2 2p^4(^1D_2)$	225.31	226.59	225.74	226.85
$1s^2 2p^4(^1S_0)$	253.94	255.12	255.07	255.86

[a] NIST critically evaluated data for atomic energy levels: http://physics.nist.gov/cgi-bin/AtData/levels_form.

TABLE 2
EXPERIMENTAL AND THEORETICAL Fe XXII TARGET ENERGIES (RELATIVE TO THE GROUND STATE) IN eV

Level	Experiment[a]	MCBP	MCDF	FAC
$1s^2 2s^2 2p(^2P^o_{1/2})$	0.0	0.0	0.0	0.0
$1s^2 2s^2 2p(^2P^o_{3/2})$	14.663	14.331	14.652	14.595
$1s^2 2s2p^2(^4P_{1/2})$	50.159	48.736	49.405	49.524
$1s^2 2s2p^2(^4P_{3/2})$	57.050	55.491	56.244	56.376
$1s^2 2s2p^2(^4P_{5/2})$	63.637	62.430	62.874	62.971
$1s^2 2s2p^2(^2D_{3/2})$	91.318	91.277	91.709	91.760
$1s^2 2s2p^2(^2D_{5/2})$	94.182	94.064	94.423	94.478
$1s^2 2s2p^2(^2P_{1/2})$	105.82	105.96	106.98	106.68
$1s^2 2s2p^2(^2S_{1/2})$	121.29	121.08	122.28	122.07
$1s^2 2s2p^2(^2P_{3/2})$	123.03	123.46	124.44	123.91
$1s^2 2p^3(^4S^o_{3/2})$	155.68	154.17	155.50	155.29
$1s^2 2p^3(^2D^o_{3/2})$	173.14	172.85	173.28	173.64
$1s^2 2p^3(^2D^o_{5/2})$	176.91	177.03	176.89	177.38
$1s^2 2p^3(^2P^o_{1/2})$	194.61	194.66	195.40	195.66
$1s^2 2p^3(^2P^o_{3/2})$	201.82	201.81	202.43	202.62

[a] NIST critically evaluated data for atomic energy levels: http://physics.nist.gov/cgi-bin/AtData/levels_form.

2. EXPERIMENTAL TECHNIQUE

DR measurements are carried out by merging, in one of the straight sections of TSR, a circulating ion beam with an electron beam. After demerging, recombined ions are separated from the stored ions using a dipole magnet and directed onto a detector. The relative electron-ion collision energy can be precisely controlled and the recombination signal measured as a function of this energy. Details of the experimental setup have been given elsewhere (Kilgus et al. 1992; Lampert et al. 1996; Savin et al. 1997, 1999, 2002b; Schippers et al. 2000, 2001). Here we discuss only those new details of the setup that were specific to our Fe XXI and Fe XXII results.

Beams of 280 MeV $^{56}Fe^{20+}$ and of 203 MeV $^{56}Fe^{21+}$ were produced and injected into TSR by the usual techniques. Stored ion currents of $\approx$35–55 μA were achieved for Fe^{20+} and $\approx$20–90 μA for Fe^{21+}. With electron cooling, the storage lifetime was $\approx$40 s for Fe^{20+} and $\approx$180 s for Fe^{21+}. After injection, the ions were cooled for $\approx$5–10 s before data collection began. This is long compared to the lifetimes of the various Fe XXI and Fe XXII metastable levels (Cheng, Kim, & Desclaux 1979), and all ions were assumed to be in their ground state for the measurements.

The electron beam was adiabatically expanded from a diameter of $\approx$0.95 cm at the electron gun cathode to $\approx$2.95 cm before it was merged with the ions. In the merged-beams region, the electrons were guided with a magnetic field of $\approx$40 mT and traveled colinear with the stored ions for a distance of $L \approx 1.5$ m. The effective energy spread associated with the relative motion between the ions and the electrons corresponds to temperatures of $k_B T_\perp \approx 14$ meV perpendicular to the confining magnetic field and $k_B T_\parallel \approx 0.15$ meV parallel to the magnetic field. The electron density varied in the range of $n_e \approx (0.6\text{–}2.8) \times 10^7$ cm^{-3} for the Fe XXI data and $n_e \approx (1.0\text{–}3.1) \times 10^7$ cm^{-3} for the Fe XXII data.

Data were collected by chopping the electron beam between the energies for cooling (E_c), measurement (E_m), and reference (E_r). The electron beam energy is chopped to both cool the ion beam and to determine the electron capture background signal at some reference energy that is free of any significant DR signal. Typically, E_r was about 50% higher than E_c. Two different chopping patterns are commonly used: either E_c-E_m-E_r or E_c-E_r-E_m. Each pattern has its particular advantage. When chopping the electron beam energy, capacitances in the electron cooler can prevent the electron beam acceleration voltage from reaching the desired value in the time allotted. This can result in the actual value of E_m differing from the programmed value, hence resulting in an incorrect calculated value for E_{cm}. Using the first pattern, charging effects are expected to be insignificant for energies where $E_m \approx E_c$. Using the second pattern, the charging effects are expected to be unimportant for energies where $E_m \approx E_r$.

For Fe XXI, an E_c-E_m-E_r chopping pattern was used with a 1.5 ms settling time following each voltage jump. After settling, data were collected for 30 ms at cooling, 20 ms at measurement, and 20 ms at reference. The pattern was repeated 500 times between injections of new ion current. With each step in the chopping pattern, E_m was changed in the lab frame by $\approx$0.5 eV (hereafter, the Fe XXIa data set). The reference energy E_r was chosen so that radiative recombination (RR) and DR contributed insignificantly to the recombination counts collected at E_r. This count rate was due to essentially only charge transfer (CT) of the ion beam off the rest gas in TSR. Taking electron beam space charge effects into account, the reference energy was $\approx$1418 eV greater than the cooling energy of $\approx$2738 eV. This corresponds to center-of-mass collision energies $E_{cm} = E_{\rm ref} \approx 147$ eV.

Data were also collected for $E_{cm} \lesssim 3.3$ eV using the same chopping pattern but a different timing, namely 30 ms at cooling, 3 ms at measurement, and 3 ms at reference (hereafter, the Fe XXIb data set). The pattern was repeated 550 times between injections of new ion current. E_m was changed in the lab frame by $\approx$0.1 eV with each step in the chopping pattern. The Fe XXIb data set was merged with the Fe XXIa data using the energy range 1.3 eV $\lesssim E_{cm} \lesssim$ 1.5 eV, which is free of any significant DR resonances. In specific, the background recombination signal of the Fe XXIb data was adjusted by a small amount to match that of the Fe XXIa data set at $E_{cm} \approx 1.4$ eV. We attribute this small difference to the use of different timings and different values of E_r for each data set. The two data sets for Fe XXI were then merged using the Fe XXIb data for $E_{cm} \lesssim 3.3$ eV and the Fe XXIa for $E_{cm} \gtrsim 3.3$ eV.

For Fe XXII, a chopping pattern of E_c-E_r-E_m was used with a 1.5 ms settling time following each voltage jump. After settling, data were collected using a timing pattern of 30 ms at cooling, 20 ms at measurement, and 20 ms at reference. The chopping pattern was repeated 500 times between injections of new ion current. With each step in the chopping pattern, E_m was changed in the lab frame by $\approx$0.5 eV (hereafter, the Fe XXIIa data set). As before, the reference energy E_r was chosen so that RR and DR contributed insignificantly to the recombination counts collected at E_r. Taking electron beam space charge effects into account, the reference energy was $\approx$1152 eV greater than the cooling energy of $\approx$1950 eV. This corresponds to center-of-mass collision energies $E_{cm} = E_{\rm ref} \approx 133$ eV.

Data were also collected for $E_{cm} \lesssim 4.6$ eV using the same chopping pattern but a different timing, namely 30 ms at cooling, 3 ms at measurement, and 3 ms at reference (hereafter, the Fe XXIIb data set). The pattern was repeated 400 times between injections of new ion current. E_m was changed in the lab frame by $\approx$0.1 eV with each step in the chopping pattern. The Fe XXIIb data set was merged with the Fe XXIIa data using the energy range 3.0 eV $\lesssim E_{\rm cm} \lesssim$ 4.0 eV, which is free of any significant DR resonances. In specific, the background recombination signal of the Fe XXIIb data was adjusted by a small amount to match that of the Fe XXIIa data set at $E_{cm} \approx 3.9$ eV. We attribute this small difference to the use of different timings and different values of E_r for each data set. The two data sets for Fe XXII were then merged using the Fe XXIIb data for $E_{cm} \lesssim 4.6$ eV and the Fe XXIIa for $E_{cm} \gtrsim 4.6$ eV.

E_{cm} was calculated from the velocities of the electrons and the ions in the overlap region. The electron velocity was calculated with the calibrated acceleration voltage and correcting for the effects of space charge in the electron beam using the beam energy and diameter and the measured beam current. The ion velocity is determined by the electron velocity at cooling. The systematic inaccuracies in the absolute E_{cm} scale derived from the voltage calibrations were $\lesssim$2%. These inaccuracies are attributed to capacitances in the electron cooler, which prevented the electron beam accelerator voltage from reaching the desired value in the time allotted.

To further increase the accuracy of the E_{cm} scale, a final normalization of the E_{cm} scale was performed using

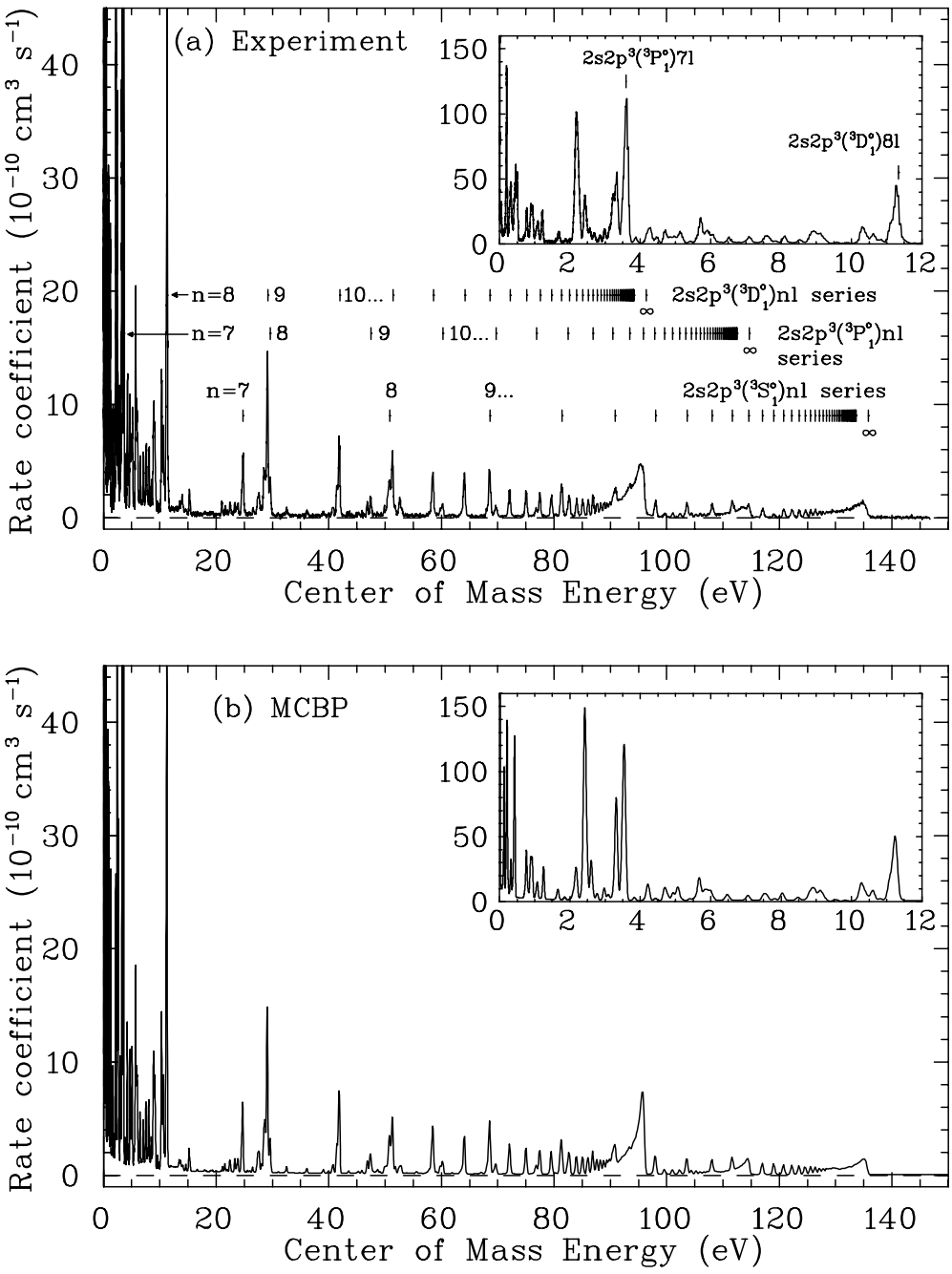

FIG. 1.—Fe XXI to Fe XX $2 \rightarrow 2$ DR resonance structure: (*a*) experimental, (*b*) MCBP, (*c*) MCDF, and (*d*) FAC results. The experimental and theoretical data represent the DR and RR cross sections times the electron-ion relative velocity convolved with the energy spread of the experiment (i.e., a rate coefficient) and are shown vs. electron-ion center-of-mass collision energy. In (*a*) resonances resulting from the $^3P_0$—$^3D^o_1$, $^3P_0$—$^3P^o_1$, and $^3P_0$—$^3S^o_1$ core excitations are labeled for capture into high *l* levels. Unlabeled resonances are due to capture into low *l* levels or due to DR via other core excitations. The nonresonant "background" rate coefficient in (*a*) is due primarily to RR. In (*b*), (*c*), and (*d*) we have added to our DR results the convolved, nonresonant RR contribution obtained from semiclassical calculations. Expanded views of selected energy ranges are shown in Fig. 6.

calculated energies for the DR resonances,

$$E_{nl} = \Delta E - \left(\frac{z}{n-\mu_l}\right)^2 \mathscr{R} \, . \qquad (4)$$

Here E_{nl} is the resonance energy for DR into a given *nl* level, *z* is the charge of the ion before DR, μ_l is the quantum defect for the recombined ion, and $\mathscr{R}$ is the Rydberg energy. Values for ΔE were taken from the NIST evaluated data for atomic energy levels and are listed in Tables 1 and 2. The quantum defects account for the energy shifts of those *l* levels that have a significant overlap with the ion core and that cannot be described using the uncorrected Rydberg formula. As *l* increases, the overlap with the ion core decreases and μ_l goes to zero.

For the normalization of the E_{cm} scale we used DR resonances with $n \geq 7$, which were essentially unblended with other resonances. We considered only the high-*l* contributions occurring at the highest energy of a given *n* manifold, for which μ_l is essentially zero. Next we calculated the ratio

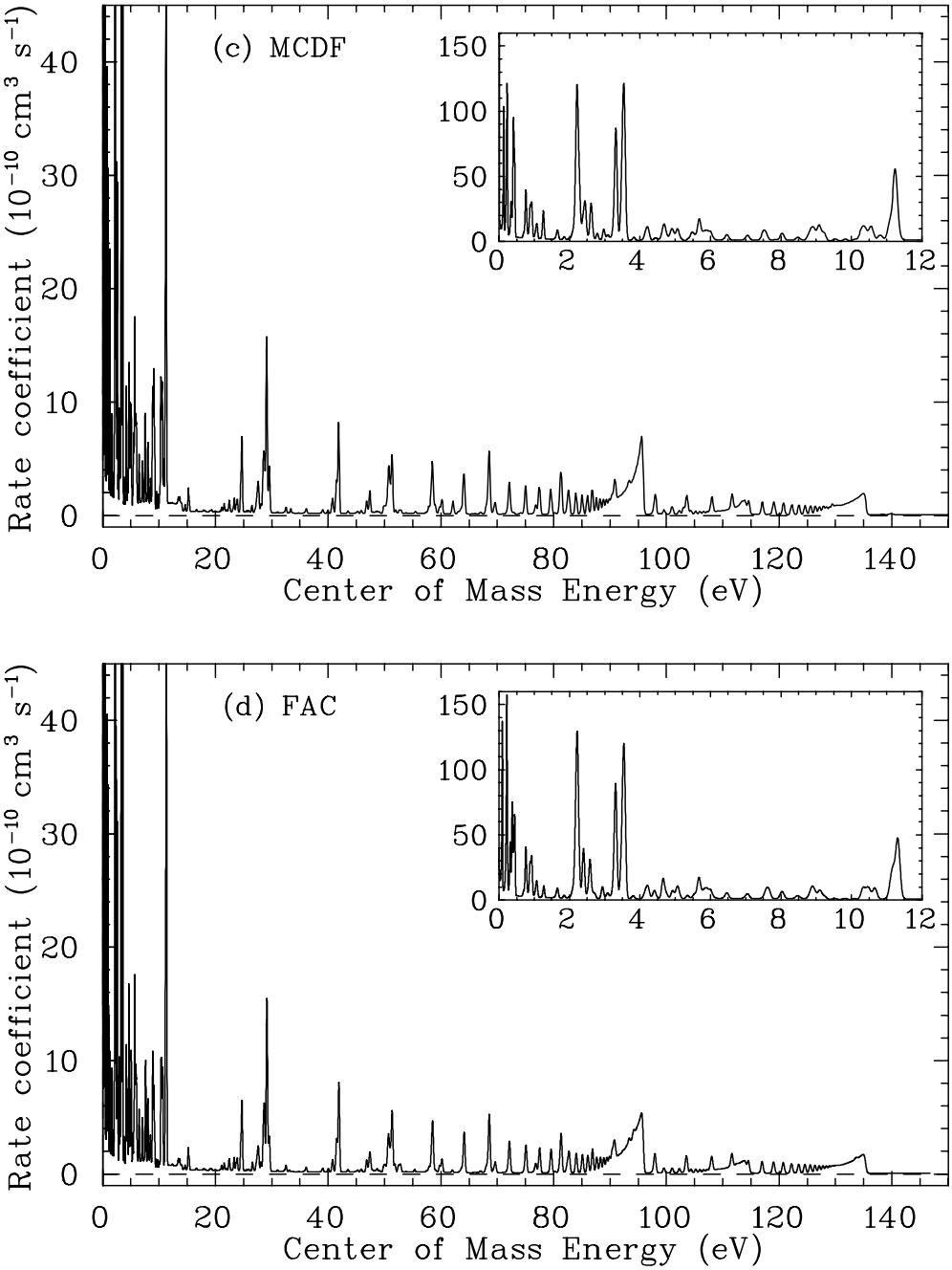

FIG. 1.—*Continued*

of E_{nl}(theory)/E_{nl}(experiment) to determine the energy-dependent normalization factor. We then used this factor to multiply the experimental energy scale in order to produce the final energy scale for the results presented here. After corrections, we estimate that the uncertainty in the corrected energy scale for both ions is as low as $\lesssim 0.5\%$.

The electron and ion beams were merged, and then, after passing through the interaction region, they were separated using toroidal magnets. Further downstream, the primary and recombined ion beams passed through two correction dipole magnets. Finally, both beams passed through a dipole which separated the recombined ions from the primary ion beam and directed the recombined ions onto a detector. Field-ionization of the recombined ions passing through these three sets of magnets has been modeled by Schippers et al. (2001). Their formalism uses the hydrogenic approximation to take into account the radiative lifetime of the Rydberg level into which the initially free electron is captured. Using this methodology, for Fe XXI we estimate that electrons captured into Rydberg levels $n_{\max} \lesssim 106$ are detected by our experimental arrangement. For Fe XXII, we estimate this is the case for $n_{\max} \lesssim 116$.

The measured recombination signal rate was calculated by taking the rate at the measurement energy $R(E_{cm})$ and subtracting from it the corresponding rate at the reference energy $R(E_{\rm ref})$. This eliminates the effects of slow pressure variations during the scanning of the measurement energy but not the effects of any fast pressure variations associated

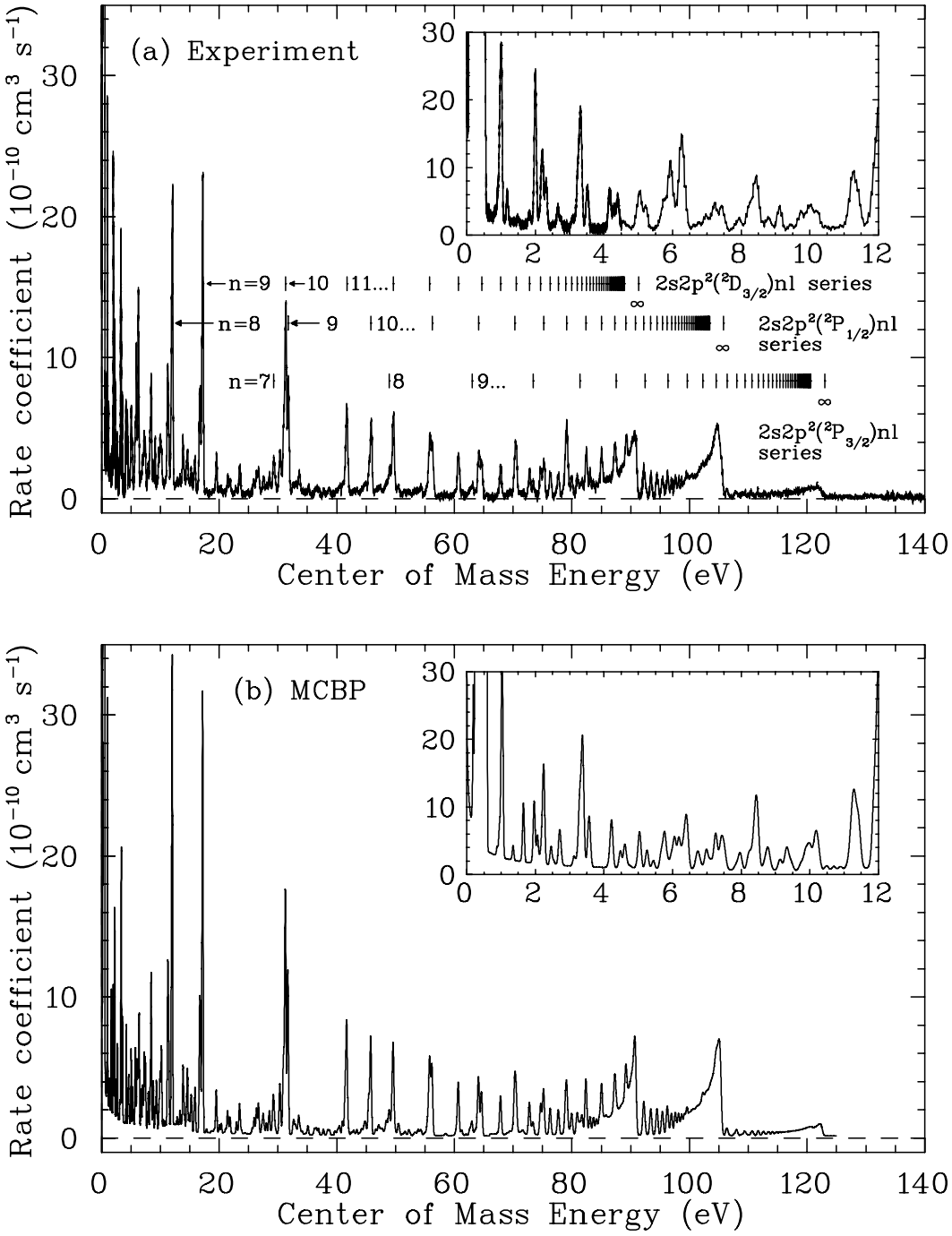

FIG. 2.—Fe XXII to Fe XXI 2 → 2 DR resonance structure: (*a*) experimental, (*b*) MCBP, (*c*) MCDF, and (*d*) FAC results. The experimental and theoretical data represent the DR and RR cross sections times the electron-ion relative velocity convolved with the energy spread of the experiment (i.e., a rate coefficient) and are shown vs. electron-ion center-of-mass collision energy. In (*a*) resonances resulting from the $^2P^o_{1/2}$—$^2D_{3/2}$, $^2P^o_{1/2}$—$^2P_{1/2}$, and $^2P^o_{1/2}$—$^2P_{3/2}$, core excitations are labeled for capture into high *l* levels. Unlabeled resonances are due to capture into low *l* levels or due to DR via other core excitations. The nonresonant "background" rate coefficient in (*a*) is due primarily to RR. In (*b*), (*c*), and (*d*) we have added to our DR results the convolved, nonresonant RR contribution obtained from semiclassical calculations. Expanded views of selected energy ranges are shown in Fig. 7.

with the chopping of the electron beam energy, leaving a small residual CT background. Following Schippers et al. (2000), the measured rate coefficient $\alpha_L(E_{cm})$ is given by

$$\alpha_L(E_{cm}) = \frac{[R(E_{cm}) - R(E_{\rm ref})]\gamma^2}{n_e N_i (L/C)\eta} + \alpha(E_{\rm ref})\frac{n_e(E_{\rm ref})}{n_e(E_{cm})} \ . \qquad (5)$$

Here N_i is the number of ions stored in the ring, $C = 55.4$ m is the circumference of the ring, η is the detection efficiency of the recombined ions (which is essentially 1), $\gamma^2 = [1 - (v/c)^2]^{-1} \approx 1.01$, and c is the speed of light. The measured rate coefficient represents the sum of the DR and RR cross sections multiplied by the relative electron-ion velocity and then convolved with the experimental energy spread. The data sit on top of the residual CT background. The experimental energy spread is best described by an aniso-

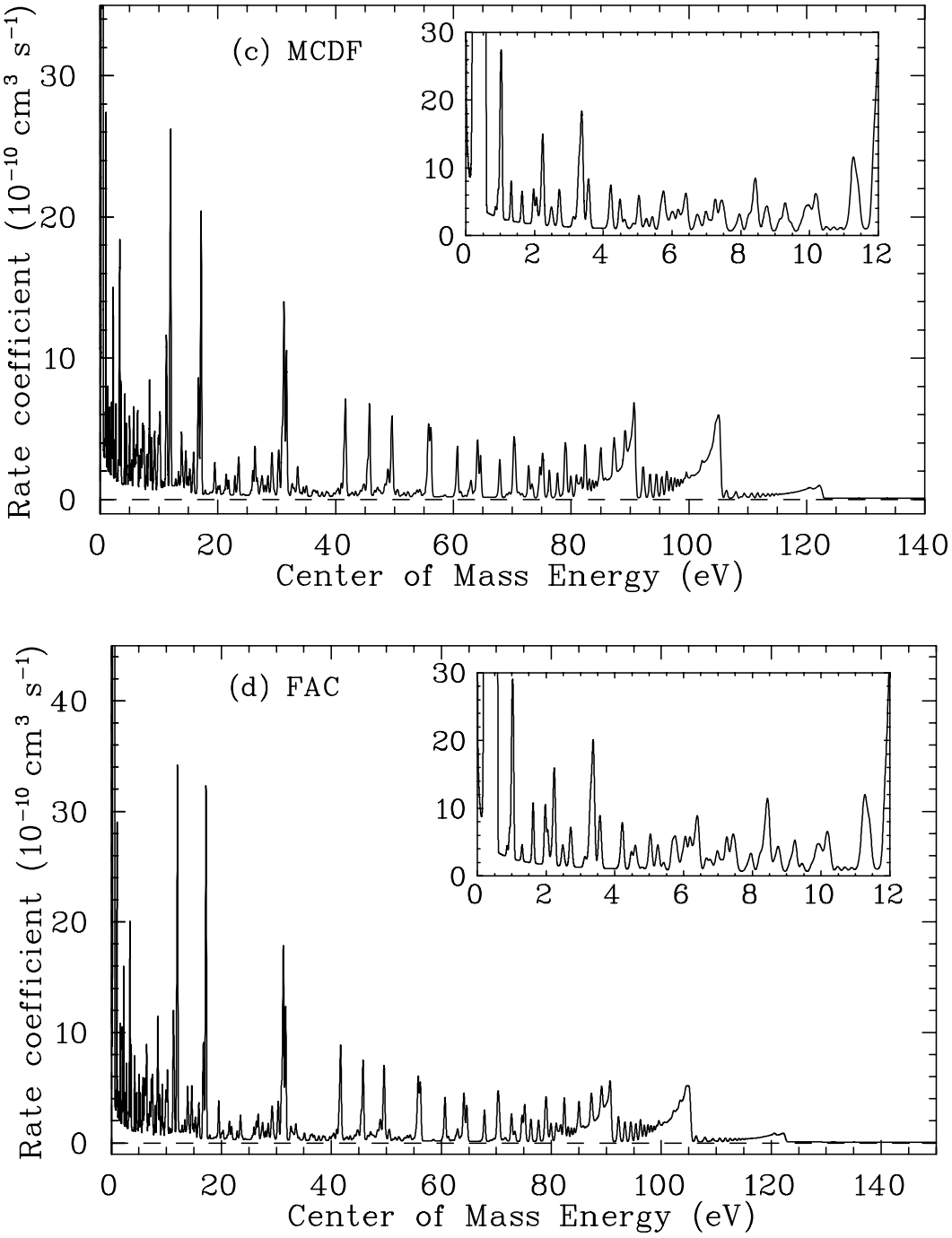

FIG. 2.—*Continued*

tropic Maxwellian distribution in the comoving frame of the electron beam. The second term in equation (5) is a small correction to re-add the RR signal at the reference which is subtracted out in the expression $[R(E_{cm}) - R(E_{\rm ref})]$. Here we used the theoretical RR rate coefficient for Fe XXI at $E_{\rm ref} = 147$ eV and for Fe XXII at $E_{\rm ref} = 133$ eV (energies here are in the center-of-mass frame). At these energies contributions due to DR are insignificant. The corresponding RR rate coefficient was calculated using a modified semiclassical formula for the RR cross section (Schippers et al. 2001). For Fe XXI, $\alpha_{\rm RR} \approx 6.3 \times 10^{-12}$ cm^3 s^{-1} and for Fe XXII, $\alpha_{\rm RR} \approx 8.1 \times 10^{-12}$ cm^3 s^{-1}. Using $\alpha_L(E_{cm})$, the effects of the merging and demerging of the electron and ion beams are accounted for, following the procedure described in Lampert et al. (1996), to produce a final measured recombination rate coefficient $\alpha(E_{cm})$ from which the DR results are extracted (e.g., Figs. 1 and 2).

The DR resonances produce peaks in $\alpha(E_{cm})$. Resonance strengths are extracted after subtracting out the smooth background due to RR and CT. RR often dominates the smooth background at low energies. In principle we can derive RR results from our data (e.g., Schippers et al. 2001), but that is beyond the scope of this paper.

Experimental uncertainties have been discussed in detail elsewhere (Kilgus et al. 1992; Lampert et al. 1996). The total systematic uncertainty in our absolute DR measurements is

estimated to be $\lesssim 20\%$. The major sources of uncertainties include the electron beam density determination, the ion current measurement, corrections for the merging and demerging of the two beams, the efficiency of the recombined ion detector, resonance strength fitting uncertainties, and uncertainties in the shape of the interpolated smooth background (particularly in regions where the DR resonances were so numerous that the background was not directly observable). Another source of uncertainty is that we assume each DR feature can be fitted using a single resonance peak when in fact each feature is often composed of many unresolved resonance peaks. Relative uncertainties for comparing our DR results at different energies are estimated to be $\lesssim 10\%$. Uncertainties are quoted at a confidence level believed to be equivalent to a 90% counting statistics confidence level.

3. EXPERIMENTAL RESULTS

Our measured $2 \rightarrow 2$ DR resonance spectrum for Fe XXI is shown in Figure 1 and for Fe XXII in Figure 2. The data represent the sum of the RR and DR cross sections times the relative electron-ion velocity convolved with the energy spread of the experiment, i.e., a rate coefficient. The data are presented as a function of E_{cm}.

In Figures 1 and 2, the strongest resonance series are those corresponding to $2s$–$2p$ core excitations. Many resonances are also seen due to other core excitations, though most of these are relatively weak. At low energies many resonances are due to core excitations involving no change in orbital configurations (e.g., $2p$–$2p$ and $2p^2$–$2p^2$ transitions). In the Fe XXI data, below ≈ 15 eV, the complexity and blending of resonances in the spectrum makes it difficult to definitively identify many of the resonances. However, a number of them lie do close in energy to the predicted resonance energies for DR via the $^3P_0$–$^3P_1$ and $^3P_0$–$^3P_2$ fine-structure core transitions. In the Fe XXII data, there is only a single fine-structure core excitation possible and the first three resonances in this series at energies of ≈ 1.1, 2.3, and 3.3 eV seem relatively identifiable, though it is likely that even these are blended with other resonance series. Overall, given the complexity of both these ions and their corresponding DR spectra, many of the resonances are actually blends from different series. Identification of the components of these blends is beyond the scope of this paper.

Due to the energy spread of the electron beam, resonances below $E_{cm} \approx k_{\rm B}T_e \approx 0.014$ eV cannot be resolved from the near 0 eV RR signal. However, we can infer the presence of such resonances in our Fe XXI data (Fig. 3), where the measured recombination rate coefficient at $E_{cm} \lesssim 10^{-4}$ eV is a factor of ≈ 26 times larger than the RR rate coefficient predicted using semiclassical RR theory with quantum mechanical corrections (Schippers et al. 2001). This is to be contrasted with Fe XXII, which is predicted and found experimentally to have no near 0 eV DR resonances. In the Fe XXII data we find an enhancement of only ≈ 2.4 for $E_{cm} \lesssim 10^{-4}$ eV. This latter enhancement is comparable to the range of enhancement factors that has been found using electron coolers on storage rings for measurements of RR for bare ions (see in Heerlein, Zwicknagel, & Toepffer 2002, Fig. 1 and references 2–12) and of DR for ions with no near 0 eV resonances (e.g., Savin et al. 1999). Hence, for the Fe XXI data, we infer the presence of at least one DR resonance at $E_{cm} < 0.014$ eV.

Our calculations predict that there is only one DR resonance below ≈ 0.014 eV and that it has a natural width significantly smaller than the resonance energy. We have tried to fit the near 0 eV feature using a single peak with both a narrow and a broad natural width. Neither fit was satisfactory. We find a best fit using three resonances, all with narrow natural widths. The largest uncertainty in our fit is due to the uncertainty in where the enhancement process turns on as E_{cm} decreases.

The measured and inferred recombination spectrum for Fe XXI below $E_{cm} = 0.1$ eV is shown in Figure 3. For the model spectrum we use our inferred and extracted resonance strengths and energies. In our fitting we have used the analytical expression from Kilgus et al. (1992) for a DR resonance with a narrow natural width convolved with the effective energy spread of the experiment. For $k_{\rm B}T_\perp$ and $k_{\rm B}T_\parallel$ we have used our extracted values. We have varied the resonance strengths for the three inferred features in our modeled recombination spectrum to achieve the best fit by eye for $0.003 \text{ eV} \lesssim E_{cm} \lesssim 0.014$ eV. Our model fit yields an enhancement factor of ≈ 1.9 for $E_{cm} \lesssim 10^{-4}$ eV. We list in Table 3 the inferred resonance strengths and energies for these three features.

We have used the predicted asymmetric line shape for the DR resonances (Anderson, Bolko, & Kvistgaard 1990; Kilgus et al. 1992) and fitted the data to extract the low-energy DR resonance strengths S_d and energies E_d for a given DR resonance or blend of resonances d. Extracted data for Fe XXI are listed in Table 3 for $E_{cm} \lesssim 1.5$ eV. The values for $k_{\rm B}T_\perp$ and $k_{\rm B}T_\parallel$ were inferred by fitting the DR peak at 0.0568 eV in the Fe XXI data. Extracted data for Fe XXII are listed in Table 4 for $E_{cm} \lesssim 0.7$ eV. Because of the complexity of the spectrum at these low energies and the discrepancies between theory and experiment (which we discuss in § 5), we have not attempted to identify the individual atomic levels responsible for the inferred and extracted resonances listed in Tables 3 and 4.

We have generated experimentally derived rate coefficients for $2 \rightarrow 2$ DR in a plasma with a Maxwellian electron energy distribution. We have done this for both Fe XXI forming Fe XX and for Fe XXII forming Fe XXI. Figure 4 shows the total $2 \rightarrow 2$ DR rate coefficient for Fe XXI calculated using the extracted and inferred data for the 0–1.5 eV range and numerically integrating the higher energy data (after subtracting out the nonresonant background). For Fe XXII we have calculated the total $2 \rightarrow 2$ DR rate coefficient using the extracted data from the 0–0.7 eV range and numerically integrating the higher energy data (after subtracting out the nonresonant background). The resulting rate coefficient is shown in Figure 5.

We estimate that the uncertainty in the absolute magnitude of our experimentally derived rate coefficients is $\lesssim 20\%$ for both Fe XXI at $k_{\rm B}T_e \gtrsim 0.5$ eV and for Fe XXII at $k_{\rm B}T_e \gtrsim 0.001$ eV. Contributions to Fe XXI (Fe XXII) DR due to capture into $n \geq n_{\rm max} = 106$ (116) are estimated to increase the $2 \rightarrow 2$ rate coefficient by less than 5% (4%) at $k_{\rm B}T_e \leq 100$ eV, and less than 8% (7%) for $100 < k_{\rm B}T_e \leq 10,000$ eV.

The accuracy of our DR rate coefficient for Fe XXI is difficult to assess for $k_{\rm B}T_e < 0.5$ eV. This is due to the difficulty of quantifying the uncertainty in the inferred, near 0 eV DR resonance strengths and energies. The contribution to the

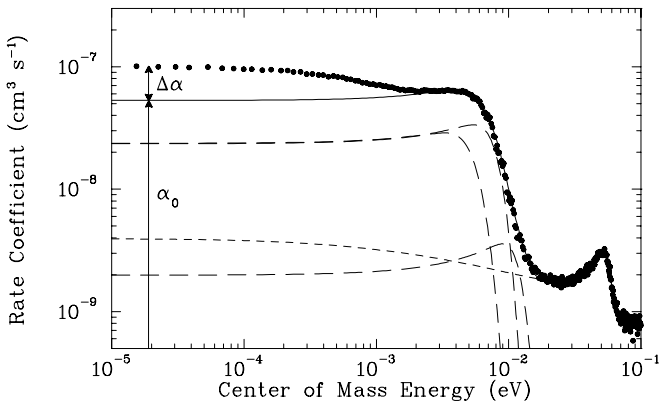

FIG. 3.—Measured and fitted Fe XXI to Fe XX $2 \rightarrow 2$ DR resonance structure below 0.1 eV. The experimental results are shown by the solid circles. The short-dashed curve is the fit to the data using our calculated RR rate coefficient and taking into account all resolved resonances. The solid curve is the fit α_0 including the estimated contributions from the unresolved near zero resonances (*long-dashed curves*; see § 3). At $E_{cm} = 10^{-5}$ eV, the difference between the model spectrum α_0 and the data is $1 + \Delta\alpha/\alpha_0 = 1.9$.

total $2 \rightarrow 2$ DR rate coefficient due to these inferred resonances is 100% for $k_B T_e \lesssim 0.01$ eV, 93% for 0.05 eV, 70% for 0.1 eV, 16% for 0.5 eV, 7% for 1 eV, and $\lesssim 1\%$ for $k_B T_e \gtrsim 5$ eV.

We have fitted our experimentally derived $2 \rightarrow 2$ DR rate coefficients using

$$\alpha_{DR}(T_e) = T_e^{-3/2} \sum_i c_i e^{-E_i/k_B T_e} , \qquad (6)$$

where T_e is given in units of kelvin. Tables 5 and 6 list the best-fit values for the fitted parameters for Fe XXI and Fe XXII, respectively. For Fe XXI, the fit is accurate to better than 0.5% for $0.001 \leq k_B T_e \leq 10,000$ eV. For Fe XXII, the fit is accurate to better than 0.5% for 0.02 eV $\lesssim k_B T_e \leq 10,000$ eV. For $k_B T_e \lesssim 0.02$ eV, the fit is larger than the experimentally derived rate coefficient. However, we expect this will have no significant effect on plasma modeling as it is extremely unlikely that Fe XXII will ever form at temperatures below 0.02 eV (Kallman & Bautista 2001) Also, both the fitted and derived rate coefficients are rapidly decreasing with decreasing energy and RR dominates the total Fe XXII electron-ion recombination rate coefficient at these low temperatures.

TABLE 3

INFERRED AND MEASURED RESONANCE ENERGIES E_d AND RESONANCE STRENGTHS S_d FOR Fe XXI TO Fe XX $2 \rightarrow 2$ DR RESONANCES FOR $E_{cm} \lesssim 1.5$ eV

Peak Number	E_d (eV)[a,b]	S_d (10^{-21} cm^2 eV)[a]
1	0.0055[c]	110000.0[c]
2	0.008[c]	110000.0[c]
3	0.012[c]	10000.0[c]
4	0.0568 ± 0.0087	3289.8 ± 40.3
5	0.2122 ± 0.0001	15224.1 ± 69.1
6	0.2958 ± 0.0004	2088.9 ± 39.2
7	0.3311 ± 0.0003	4645.4 ± 57.7
8	0.3643 ± 0.0009	1736.9 ± 65.0
9	0.4295 ± 0.0005	2661.2 ± 49.2
10	0.4690 ± 0.0002	5279.8 ± 45.9
11	0.5150 ± 0.0002	4738.6 ± 36.6
12	0.7122 ± 0.0014	328.4 ± 15.8
13	0.7789 ± 0.0004	1823.6 ± 72.5
14	0.8082 ± 0.0029	762.1 ± 71.4
15	0.9007 ± 0.0004	2116.5 ± 27.0
16	0.9513 ± 0.0003	2298.7 ± 24.4
17	1.0553 ± 0.0012	772.0 ± 25.3
18	1.1075 ± 0.0007	1332.5 ± 31.5
19	1.2280 ± 0.0003	1856.9 ± 19.3

[a] 1 σ statistical fitting uncertainties.

[b] In addition to the fitting uncertainty shown, the absolute energy scale has an uncertainty estimated to be $\lesssim 0.5\%$.

[c] Inferred values.

TABLE 4

MEASURED RESONANCE ENERGIES E_d AND RESONANCE STRENGTHS S_d FOR Fe XXII TO Fe XXI $2 \rightarrow 2$ DR RESONANCES FOR $E_{cm} \lesssim 0.7$ eV

Peak Number	E_d (eV)[a,b]	S_d (10^{-21} cm^2 eV)[a]
1	0.0885 ± 0.0001	19509.7 ± 128.8
2	0.1359 ± 0.0002	12835.1 ± 119.4
3	0.1944 ± 0.0002	27498.9 ± 264.1
4	0.2277 ± 0.0001	41089.3 ± 538.8
5	0.3152 ± 0.0007	13358.3 ± 1463.2
6	0.3553 ± 0.0006	17873.3 ± 928.3
7	0.4165 ± 0.0003	24073.0 ± 196.8
8	0.4667 ± 0.0003	33058.2 ± 199.4
9	0.5163 ± 0.0001	38810.9 ± 185.4

[a] 1 σ statistical fitting uncertainties.

[b] In addition to the fitting uncertainty shown, the absolute energy scale has an uncertainty estimated to be $\lesssim 0.5\%$.

4. THEORY

Existing theoretical rate coefficients for DR of Fe XXI and Fe XXII have been calculated by a number of different groups. Jacobs et al. (1977) presented *LS*-coupling results for Fe XXI and Fe XXII. Roszman used *LS*-coupling for Fe XXI. These results were published by Arnaud & Raymond (1992). Details on the technique used by Roszman are given in Roszman (1987). For Fe XXII, Badnell (1986) used the Burgess (1965) formula, Ramadan & Hahn (1989) used *LS*-coupling, and Chen et al. (1998) used the MCDF method. These published $2 \rightarrow 2$ DR rate coefficients for Fe XXI and Fe XXII are shown in Figures 4 and 5, respectively.

There have been major theoretical advances in the study of DR since the works of Burgess, Jacobs et al., and Roszman. We have carried out new calculations using three different state-of-the-art theoretical techniques. These methods use the independent processes and isolated resonance approximations (Seaton & Storey 1976). We expect interference between DR and RR to be unimportant for the systems studied here. In the approximations used here the interference between DR and RR is neglected and the effects of interacting resonances were ignored. The DR cross section can then be written as a product of the resonance capture cross section (which is related by detailed balance to the autoionization rate) and the stabilizing radiative branching ratio. Below we briefly describe these techniques and the results.

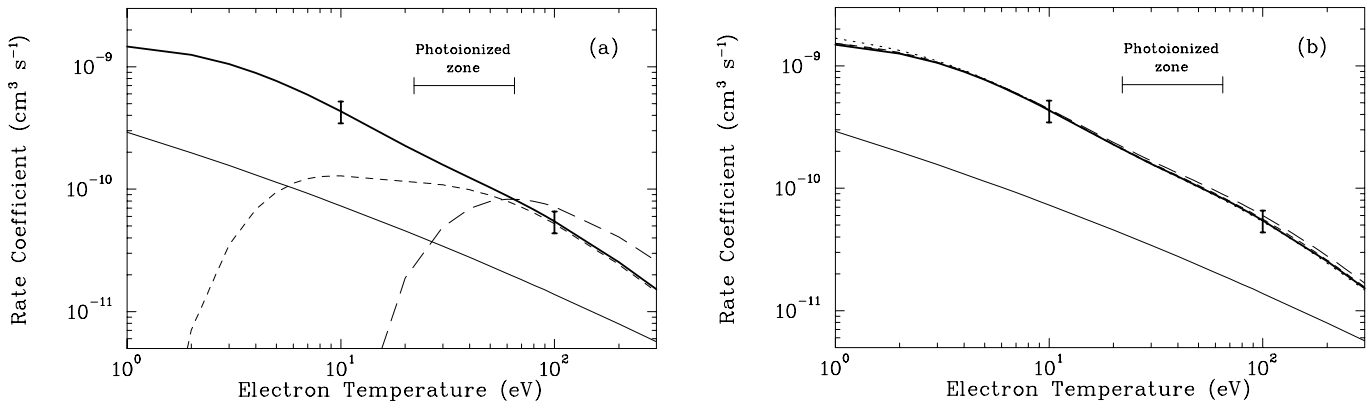

FIG. 4.—Fe XXI to Fe XX Maxwellian-averaged rate coefficient for $2 \rightarrow 2$ DR from $k_B T_e = 1$ to 300 eV. (*a*) The thick solid curve represents our experimentally derived rate coefficient using the results shown in Fig. 1*a*. The error bars represent the estimated maximum experimental uncertainty of 20% for $k_B T_e \geq 0.5$ eV. The long-dashed curve shows the *LS*-coupling calculations of Jacobs et al. (1977) as fitted by Shull & van Steenberg (1982). The short-dashed curve shows the unpublished *LS*-coupling calculations of Roszman as given by Arnaud & Raymond (1992). Also shown is the recommended RR rate coefficient of Arnaud & Raymond (1992; *thin solid curve*). (*b*) In addition to our experimentally derived DR rate coefficient (*thick solid curve*) and the recommended RR rate coefficient (*thin solid curve*), we also show our MCBP (*dotted curve*), MCDF (*long-dashed curve*), and FAC (*short-dashed curve*) results. All DR rate coefficients in (*b*) are for an $n_{max} = 106$. The formation zone of Fe XXI as predicted by XSTAR (Kallman & Bautista 2001) for an optically thin, low-density photoionized plasma of cosmic abundances is shown by the thin horizontal solid line in both (*a*) and (*b*).

4.1. *Multiconfiguration Breit-Pauli* (*MCBP*)

DR cross section calculations using the MCBP code AUTOSTRUCTURE (Badnell 1986) are based on lowest order perturbation theory, where both the electron-electron and electron-photon interactions are treated to first order. This technique has been detailed more fully in Savin et al. (2002a) for the case of Fe XX ions. However, brief descriptions of the particulars for Fe XXI and Fe XXII are given below.

4.1.1. Fe XXI

A bound orbital basis $\{1s, 2s, 2p\}$ was generated from a Hartree-Fock (Froese-Fischer 1991) calculation for the $1s^2 2s^2 2p^2$ configuration-averaged ^3P ground state of Fe XXI. Then the corresponding atomic structures for both the Fe XXI target states and the Fe XX continuum (or resonance) states were obtained by diagonalizing the appropriate Breit-Pauli Hamiltonians. Calculated ionic Fe XXI energies are listed in Table 1. Prior to the final DR cross section calculations, these ionic thresholds were shifted to the known spectroscopic values by a small amount—typically less than 2 eV. The spectroscopic values are taken from the NIST evaluated data for atomic energy levels. Distorted wave calculations were then performed to generate the appropriate free ϵl and bound nl orbitals that are attached to each target state to yield the Fe XXI continuum and resonance states, respectively. All of the above orbitals are computed in the absence of any relativistic effects. However, the continuum and resonance states are subsequently recoupled to an intermediate coupling scheme in order to include relativistic effects to lowest order. We included all possible $2s^2 2p^2 nl$, $2s2p^3 nl$, and $2p^4 nl$ resonance configurations, with

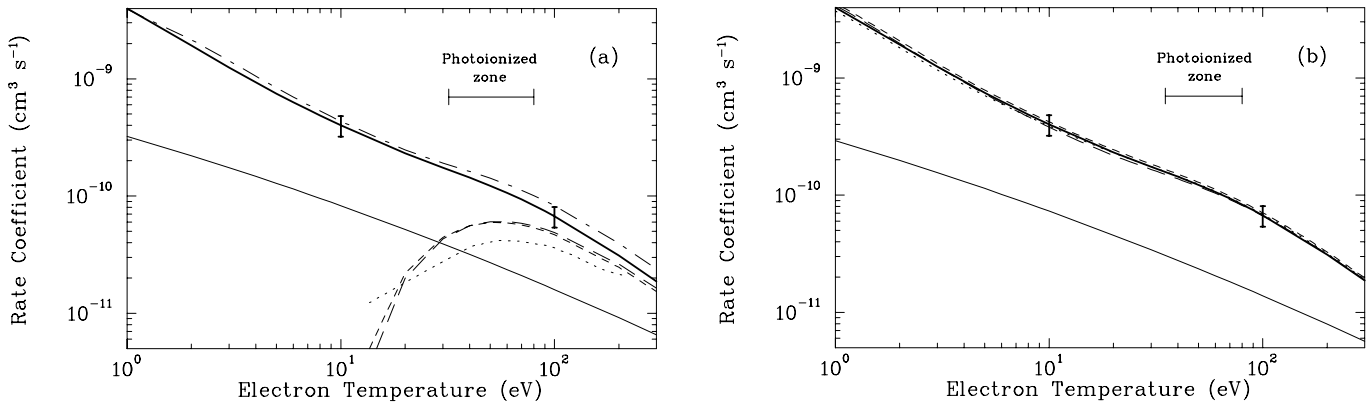

FIG. 5.—Fe XXII to Fe XXI Maxwellian-averaged rate coefficient for $2 \rightarrow 2$ DR from $k_B T_e = 1$ to 300 eV. (*a*) The thick solid curve represents our experimentally derived rate coefficient using the results shown in Fig. 2*a*. The error bars represent the estimated maximum experimental uncertainty of 20%. The long-dashed curve shows the *LS*-coupling calculations of Jacobs et al. (1977) as fitted by Shull & van Steenberg (1982). The short-dashed curve shows the Burgess formula results of Badnell (1986) as given by Arnaud & Raymond (1992). The *LS* results of Ramadan & Hahn (1989) is given by the dotted curve. Our earlier MCDF results (Chen et al. 1998) are plotted using the long-dash-dotted curve for an $n_{max} = 400$. Also shown is the recommended RR rate coefficient of Arnaud & Raymond (1992; *thin solid curve*). (*b*) In addition to our experimentally derived DR rate coefficient (*thick solid curve*) and the recommended RR rate coefficient (*thin solid curve*) we also show our MCBP (*dotted curve*), new MCDF (*long-dashed curve*), and FAC (*short-dashed curve*) results. All DR rate coefficients in (*b*) are for an $n_{max} = 116$. The formation zone of Fe XXII as predicted by XSTAR (Kallman & Bautista 2001) for an optically thin, low-density photoionized plasma of cosmic abundances is shown by the thin horizontal solid line in both (*a*) and (*b*).

TABLE 5
RATE COEFFICIENT FITTED PARAMETERS FOR 2 → 2 DR OF Fe XXI FORMING Fe XX

Parameter	Experiment	MCBP	MCDF	FAC
c_1.....	7.71E−5	2.62E−4	1.28E−4	1.51E−4
c_2.....	6.08E−5	5.04E−4	2.80E−4	4.82E−4
c_3.....	3.93E−4	1.26E−3	8.20E−4	7.60E−4
c_4.....	1.14E−3	1.02E−2	1.83E−3	1.72E−3
c_5.....	7.63E−3	1.40E−2	1.19E−2	1.13E−2
c_6.....	1.37E−2	2.16E−2	1.56E−2	1.35E−2
c_7.....	2.08E−2	7.88E−2	2.82E−2	2.05E−2
c_8.....	7.86E−2	0.00E+0	8.68E−2	8.39E−2
E_1.....	5.82E−3	3.00E−2	8.80E−3	1.00E−1
E_2.....	9.87E−3	1.96E−1	1.61E−1	2.40E−1
E_3.....	2.09E−1	5.82E−1	3.91E−1	4.75E−1
E_4.....	5.78E−1	2.64E+0	1.26E+0	1.35E+0
E_5.....	2.36E+0	7.63E+0	3.18E+0	3.16E+0
E_6.....	5.80E+0	3.17E+1	1.00E+1	8.92E+0
E_7.....	2.41E+1	9.88E+1	4.03E+1	3.24E+1
E_8.....	9.59E+1	0.00E+0	1.04E+2	9.68E+1

NOTES.—The experimental results are for $n_{max} = 106$, the MCBP results for $n_{max} = 1000$, the MCDF results for $n_{max} = 400$, and the FAC results for $n_{max} = 400$. The units are cm^3 s^{-1} K$^{1.5}$ for c_i and eV for E_i.

$2 \le n \le 1000$ and $0 \le l \le 15$, and all corresponding continuum configurations $2s^2 2p^2 \epsilon l$, $2s2p^3\epsilon l$, and $2p^4\epsilon l$. To account for field ionization effects, we also eliminated all resonances with $n > 106$.

In the MCBP calculations, it is normally assumed that resonances which radiate to autoionizing states will not contribute to the DR cross section. This has usually been found to be a good approximation since the radiative branching ratio of such states is typically very small. In the present cases of Fe XXI and Fe XXII however, we find that the radiative branching ratios are nonnegligible and that when we include this two-step radiative cascade contribution, the DR cross section near the highest thresholds is increased by factors of 2 or more.

TABLE 6
RATE COEFFICIENT FITTED PARAMETERS FOR 2 → 2 DR OF Fe XXII FORMING Fe XXI

Parameter	Experiment	MCBP	MCDF	FAC
c_1.....	1.46E−4	5.01E−6	4.96E−6	2.00E−4
c_2.....	1.17E−3	4.23E−5	1.01E−4	1.93E−3
c_3.....	4.22E−3	1.51E−3	1.75E−3	5.93E−3
c_4.....	2.80E−3	5.62E−3	6.12E−3	7.99E−4
c_5.....	9.22E−3	5.75E−3	5.71E−3	3.39E−3
c_6.....	3.13E−2	3.12E−2	2.86E−2	1.69E−2
c_7.....	9.98E−2	1.08E−1	1.19E−1	3.35E−2
c_8.....	0.00E+0	0.00E+0	0.00E+0	1.04E−1
E_1.....	1.36E−1	1.83E−1	1.80E−1	2.10E−1
E_2.....	2.09E−1	2.01E−1	2.08E−1	2.93E−1
E_3.....	4.18E−1	2.96E−1	2.84E−1	5.17E−1
E_4.....	9.35E−1	5.22E−1	5.12E−1	1.27E+0
E_5.....	6.14E+0	4.12E+0	4.40E+0	4.12E+0
E_6.....	2.34E+1	1.87E+1	2.01E+1	1.19E+1
E_7.....	8.55E+1	8.22E+1	8.57E+1	3.52E+1
E_8.....	0.00E+0	0.00E+0	0.00E+0	9.10E+1

NOTES.—The experimental results are for $n_{max} = 116$, the MCBP results for $n_{max} = 1000$, the MCDF results for $n_{max} = 400$, and the FAC results for $n_{max} = 400$. The units are cm^3 s^{-1} K$^{1.5}$ for c_i and eV for E_i.

4.1.2. Fe XXII

The only differences between the calculations for Fe XXII, compared to Fe XXI, is that now we determine the $\{1s, 2s, 2p\}$ orbitals from a Hartree-Fock calculation for the $1s^2 2s^2 2p(^2P)$ state and include the configurations $2s^2 2pnl$, $2s2p^2nl$, and $2p^3nl$, with $2 \le n \le 1000$ and $0 \le l \le 15$, for the resonance states, and $2s^2 2p\epsilon l$, $2s2p^3\epsilon l$, and $2p^4\epsilon l$ for the continuum states. The Fe XXII target energies, prior to shifting, are given in Table 2. To account for field ionization effects, we also eliminated all resonances with $n > 116$.

4.2. *Multiconfiguration Dirac-Fock* (*MCDF*)

The required transition energies, Auger rates, and radiative transition rates were evaluated using the MCDF method (Grant et al. 1980; Chen 1985) in intermediate coupling with configuration interaction from the same complex. Both rates were calculated from first-order perturbation theory. In the calculations of Auger matrix elements, we included the contributions from not only the two-electron operator but also the one-electron operator. For the $2 \to 2$ transitions with $2s$–$2p$ and $2p_{1/2}$–$2p_{3/2}$ excitations, explicit calculations were performed for intermediate states with $n \le 30$ and $l \le 12$. Since many important resonances have very small energies, the resonance energies were adjusted by using the known experimental excitation energies between $N = 2$ states (using the NIST evaluated database). The contributions from the high-n Rydberg states were taken into account using an n^{-3} scaling for the appropriate Auger and radiative transition rates up to $n = 400$.

For the case of $2s$–$2p$ excitations, the radiative decay of the $2p$ electron can lead to an autoionizing state. For these DR transitions, a one-step cascade correction was included. We also included the contributions from $1s^2 2p^4 nl$ intermediate states for Fe XXI and $1s^2 2p^3 nl$ intermediate states for Fe XXII. These intermediate states were made possible by the ground state correlations.

The inclusion of $1s^2 2p^4 nl$ and $1s^2 2p^3 nl$ autoionizing states in Fe XXI and Fe XXII, respectively, can produce a whole series of new features in the calculated DR spectra. Here we just mention a few of them. For Fe XXI, the peaks at 52.5, 56.0, and 59.1 eV can be identified as due to $1s^2 2p^4 6l$ resonances. For Fe XXII, the peaks at 1.32, 1.62, 2.5, and 23.5 eV are from $1s^2 2p^3 6l$ resonances. The effects on the $2 \to 2$ DR rate coefficients, however, are quite small. They change the rate coefficients by $<1\%$ for Fe XXI and $\lesssim 2\%$ for Fe XXII.

For Fe XXII, the new MCDF calculations included contributions from the one-electron operator and intermediate states made possible by ground state correlations that were neglected in our early MCDF calculations (Chen et al. 1998). In addition, our new MCDF calculations used the NIST recommended $2p_{1/2}$–$2p_{3/2}$ excitation energy, while the earlier MCDF results used our calculated theoretical value.

4.3. *Flexible Atomic Code* (*FAC*)

FAC is a relativistic, configuration interaction program for calculating various atomic collisional and radiative processes, including Auger rates and radiative transition rates, which are needed to obtain DR cross sections (Gu

2003b). The theoretical method employed in FAC is quite similar to that of AUTOSTRUCTURE, except that the Dirac-Coulomb Hamiltonian is used for the construction of radial wave functions and the evaluation of Hamiltonian matrix elements. The difference between FAC and MCDF is that the single electron wave function basis is obtained with an optimized effective potential instead of the multiconfiguration variational procedure. Both Auger rates and radiative transition rates are evaluated in the first-order perturbation theory. Explicit calculations are performed for doubly excited states with $n \leq 50$ and $l \leq 12$. Contributions from higher n states (up to $n = 400$) are taken into account using the hydrogenic scaling laws of Auger and radiative transition rates. As in the previous two methods, the resonance energies are empirically adjusted using the NIST recommended excitation energies of $2 \rightarrow 2$ transitions of Fe XXI and Fe XXII.

For both Fe XXI and Fe XXII, configuration interaction within same complexes are allowed. Radiative cascades to autoionizing states are fully taken into account using an iterative procedure to calculate the radiative stabilizing branching ratio:

$$B_i = \frac{\sum_j A^r_{ij} + \sum_{i'} A^r_{ii'} B_{i'}}{\sum_j A^a_{ij} + \sum_k A^r_{ik}} , \quad (7)$$

where A^r_{ij} is the radiative decay rate from state i to state j, A^a_{ik} is the autoionization rate from state i to state k, and state i' may further autoionize and has a stabilizing branching ratio of $B_{i'}$.

4.4. *Results*

For the MCBP, MCDF, and FAC results, the DR cross section was approximated by the sum of Lorentzian profiles for each included resonance. This analytic cross section was convolved with the experimental energy distribution for comparison with the measured results. The convolved results are presented in Figures 1 and 2 for Fe XXI and Fe XXII, respectively.

Total $2 \rightarrow 2$ DR rate coefficients were obtained by convolving the DR cross section with a Maxwellian electron distribution. The resulting Maxwellian rate coefficients are given in Figures 4 and 5 for Fe XXI and Fe XXII, respectively. For the Fe XXI results we have used $n_{\max} = 106$ and for the Fe XXII results $n_{\max} = 116$.

We have fitted the theoretical total $2 \rightarrow 2$ DR rate coefficients using equation (6). Fitted parameters for Fe XXI and Fe XXII are given in Tables 5 and 6, respectively. Here we have fitted the rate coefficients for the cases of $n_{\max} = 1000$ for the MCBP results and $n_{\max} = 400$ for the MCDF and FAC results. Contributions due to higher n levels are expected to have an insignificant effect on the total $2 \rightarrow 2$ DR rate coefficient.

For Fe XXI in the temperature range $0.001 \leq k_B T_e \leq 10,000$ eV, the fit to the MCBP rate coefficient is accurate to better than 0.6% and for the MCDF data to better than 0.3%. For the FAC data the fit is accurate to better than 1% for $0.04 \leq k_B T_e \leq 10,000$ eV. Below 0.04 eV the fit is significantly worse, but this is not expected to be a problem for plasma modeling as it is extremely unlikely that Fe XXI will ever form below this temperature (Kallman & Bautista 2001). Also, there are more important atomic physics issues relating to the reliability of the theoretical DR rate coefficients at these low temperatures, which we discuss in the next section.

For Fe XXI, the fit to the MCBP rate coefficient is accurate to better than 2.5% for $0.006 \text{ eV} \leq k_B T_e \leq 10,000$ eV. For the MCDF rate coefficient the fit is accurate to better than 3% for $0.002 \text{ eV} \leq k_B T_e \leq 10,000$ eV. For the FAC data the fit is accurate to better than 1% for $0.02 \text{ eV} \leq k_B T_e \leq 10,000$ eV. All three fits are less good for temperatures below the lower limits quoted here. However, this is not expected to be a problem for plasma modeling as it is extremely unlikely that Fe XXII will ever form at temperatures below these lower limits (Kallman & Bautista 2001). Also, the fitted rate coefficients are rapidly decreasing with decreasing temperature and RR is expected to dominate the total electron-ion recombination rate coefficient at these low temperatures.

5. DISCUSSION

5.1. *Resonance Structure*

In Figures 6 and 7 we have plotted, for both Fe XXI and Fe XXII, respectively, the energy regimes where the largest discrepancies between theory and experiment occur. In these plots we show the measured rate coefficients and the theoretical results convolved with the experimental energy spread. As we have found in the past, many of the discrepancies tend to occur for collision energies below ≈ 3 eV. The dramatic difference between the measured and theoretical resonance structure below ≈ 1 eV has made it difficult to make assignments for the extracted resonances listed in Tables 3 and 4. The agreement between our experimental and theoretical results is significantly better for energies $\gtrsim 3$ eV.

Accurately calculating the DR resonance structure using a single theoretical technique over the entire energy range of resonances remains one of the biggest challenges for DR theory. No theoretical technique currently exists which is capable of reliably calculating the resonance structure at both low energies ($\lesssim 3$ eV) and at higher energies ($\gtrsim 3$ eV). Relativistic many-body perturbation theory has been used successfully to match the low-energy DR resonance structure, but only for the relatively simple lithium-like ions (e.g., Mohamed et al. 2002; Tokman et al. 2002). This technique has yet to be applied to more complicated systems such as the carbon-like and boron-like ions studied here. MCBP, MCDF, FAC, and *R*-matrix results have been successful in matching the measured resonance structure for energies $\gtrsim 3$ eV (e.g., Savin et al. 2002a, 2002b; Gorczyca, Badnell, & Savin 2002) but are less successful for lower energies.

5.2. *Rate Coefficients*

None of the LS-coupling or Burgess formula results published prior to our measurements reliably reproduce the magnitude and temperature dependence of our experimentally derived $2 \rightarrow 2$ DR rate coefficients. Our earlier Fe XXII MCDF results are in good agreement with our experimental results for $k_B T_e \gtrsim 0.06$ eV.

As for our new calculations, our MCBP results are in excellent agreement with our experimental-derived rate coefficient at $k_B T_e \gtrsim 0.7$ eV for Fe XXI and $k_B T_e \gtrsim 0.3$ eV for Fe XXII. Our new MCDF results are in excellent agreement with our experimental results at $k_B T_e \gtrsim 0.02$ eV for Fe XXI and at $k_B T_e \gtrsim 0.2$ eV for Fe XXII. Our FAC results are in

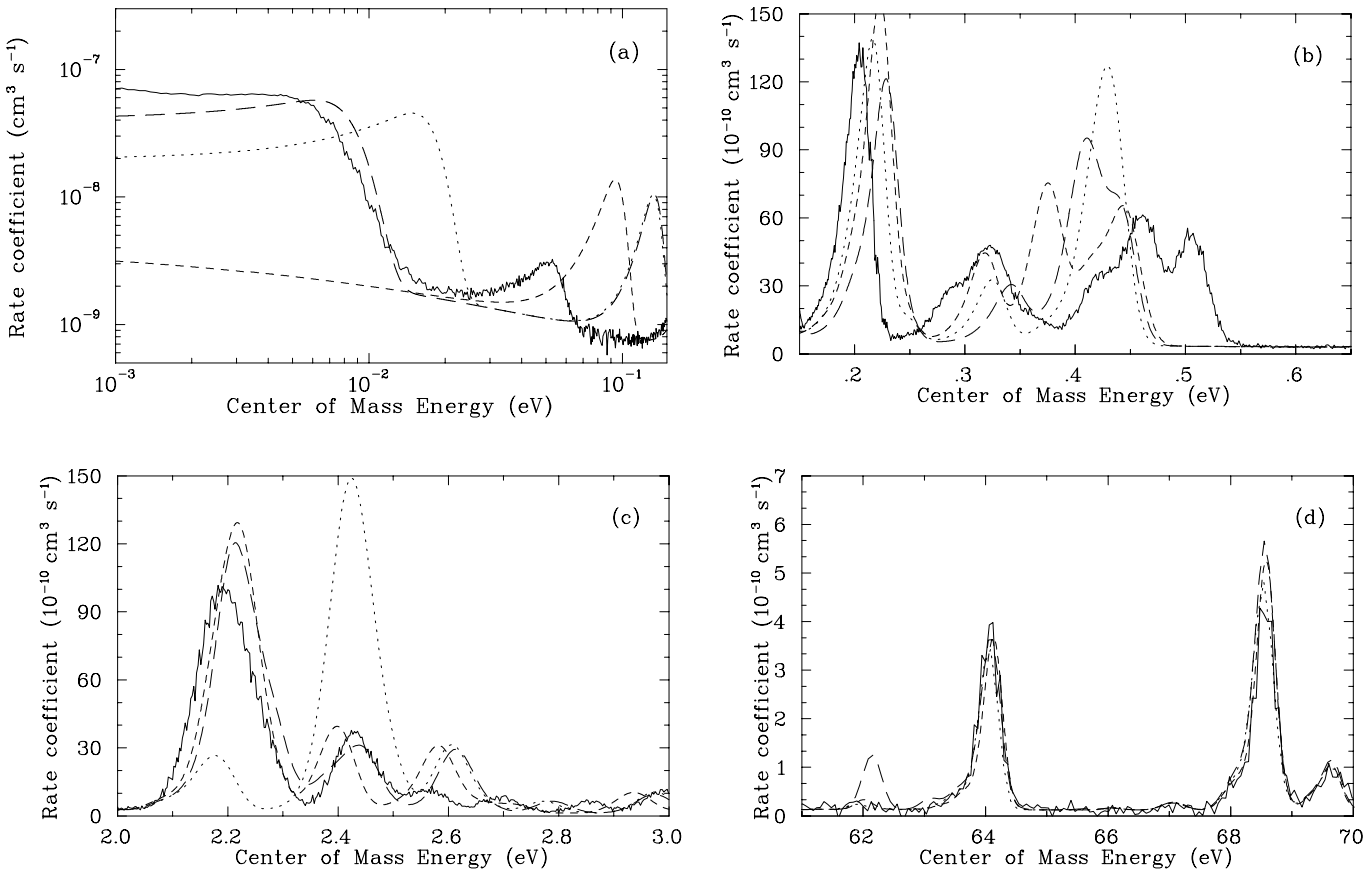

FIG. 6.—Expanded views of selected energy ranges for the Fe XXI data from Fig. 1. Here we show the experimental results (*solid curve*), the MCBP results (*dotted curve*), the MCDF results (*long-dashed curve*), and the FAC results (*short-dashed curve*) in those energy ranges exhibiting significant discrepancies between theory and experiment. In (*a*) the energy range is from 0.001 to 0.15 eV. The MCPB, MCDF, and FAC results do not include the effects of the recombination enhancement below ≈0.002 eV. In (*b*) the energy range is from 0.15 to 0.65 eV, in (*c*) from 2.0 to 3.0 eV, and in (*d*) from 61 to 70 eV.

excellent agreement with the experimental data at $k_B T_e \gtrsim 0.2$ eV for both Fe XXI and Fe XXII.

Our experimentally derived $2 \rightarrow 2$ DR rate coefficients are accurate over a range in temperature that includes the ≈20–80 eV range where Fe XXI and Fe XXII are predicted to form in an X-ray photoionized plasma of cosmic abundances (Kallman & Bautista 2001). At plasma temperatures $\gtrsim 150$ eV, one needs to begin to account for the contribution of $2 \rightarrow 3$ DR to the total DR rate coefficients (Arnaud & Raymond 1992).

5.3. *Implications for Plasma Modeling*

Our measurements provide important benchmarks for state-of-the-art DR theory. By comparison with our experimental results, theorists are able to determine which approximations and processes need to be included in their calculations to reach good agreement with experiment. Using this benchmarked theory it should now be possible to produce with a high degree of reliability DR rate coefficients for the many other astrophysically important ions in the measured carbon-like and boron-like isoelectronic sequences. The only caveat is that MCBP, MCDF, and FAC results will not be able to reproduce reliably the DR resonance strengths and energies for relative collision energies $\lesssim 3$ eV (cf. Figs. 6 and 7). For carbon-like and boron-like ions which form at temperatures where these resonances are important, laboratory measurements are the only way at present to produce reliable DR data.

6. CONCLUSIONS

We have measured the $2 \rightarrow 2$ DR resonance structure for Fe XXI forming Fe XX and for Fe XXII forming Fe XXI. In general for $E_{cm} \gtrsim 3$ eV we find good agreement between our experimental and results and our MCBP, MCDF, and FAC results. We have used our measured resonance spectra to produce experimentally derived $2 \rightarrow 2$ DR rate coefficients. Previous published Burgess formula and LS-coupling calculations are in poor agreement with our experimentally derived rate coefficients. None of these published calculations reliably reproduce the magnitude or temperature dependence of our experimental results. Our previously published Fe XXI MCDF results are in good agreement with our experimental results for $k_B T_e \gtrsim 0.07$ eV. For both ions our new MCBP, MCDF, and FAC results are in excellent agreement with our experimentally derived rate coefficient for $k_B T_e \gtrsim 0.02$–0.7 eV.

We would like to thank P. Richard for stimulating discussions during the beam time. This work was supported in part by NASA High Energy Astrophysics X-Ray Astronomy Research and Analysis grant NAG5-5123 and NASA Space Astrophysics Research and Analysis Program grant NAG5-5261. Travel to and living expenses at TSR for

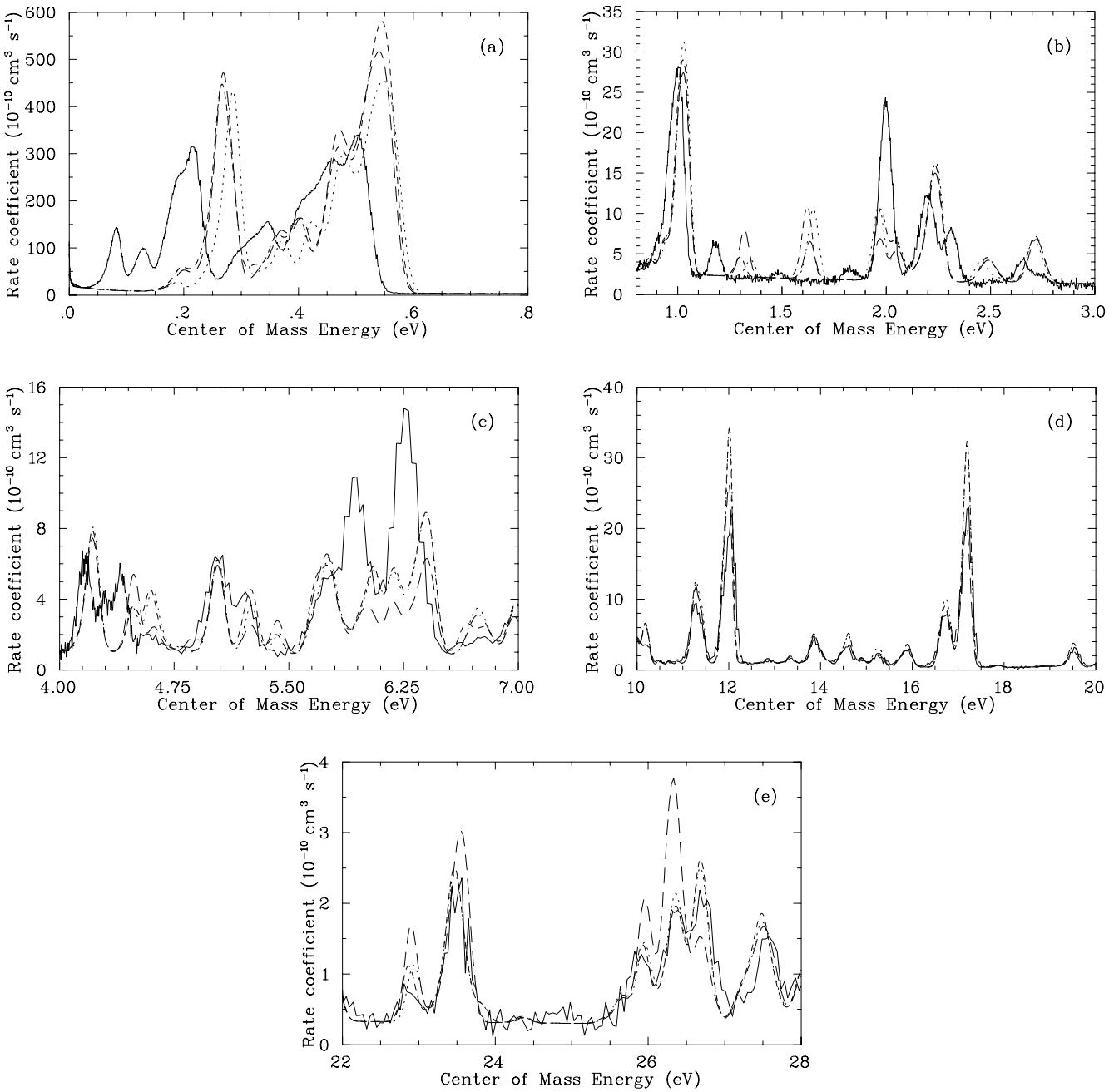

FIG. 7.—Expanded views of selected energy ranges for the Fe XXII data from Fig. 2. Here we show the experimental results (*solid curve*), the MCBP results (*dotted curve*), the MCDF results (*long-dashed curve*), and the FAC results (*short-dashed curve*) in those energy ranges exhibiting significant discrepancies between theory and experiment. The energy ranges shown are (*a*) 0.0–0.8 eV, (*b*) 0.8–3.0 eV, (*c*) 4.0–7.0 eV, (*d*) 10–20 eV, and (*e*) 22–28 eV.

D. W. S. and P. A. Z. were funded by NATO Collaborative Research grant CRG-950911. Work performed in Germany has been supported in part by the German Federal Minister for Education and Research (BMBF) under contracts 06 GI 475, 06 GI 848, and 06 HD 854I and the German Research Council (DFG, Bonn–Bad Godesberg) under project number MU 1068/8. Work performed at Lawrence Livermore National Laboratory was carried out under the auspices of the US Department of Energy by the University of California, Lawrence Livermore National Laboratory, under contract W-7405-ENG-48. T. W. G. and O. Z. were supported in part by NASA Space Astrophysics Research and Analysis Program grant NAG5-10448. M. F. G. was supported by NASA through *Chandra* Postdoctoral Fellowship Award Number PF01-10014 issued by the *Chandra X-ray Observatory* Center, which is operated by the Smithsonian Astrophysical Observatory for and on behalf of NASA under contract NAS8-39073.

REFERENCES

Andersen, L. H., Bolko, J., & Kvistgaard, P. 1990, Phys. Rev. A, 41, 1293
Arnaud, M., & Raymond, J. C. 1992, ApJ, 398, 394
Badnell, N. R. 1986, J. Phys. B, 19, 3827
Burgess, A. 1965, ApJ, 141, 1588
Chen, M. H. 1985, Phys. Rev. A, 31, 1449
Chen, M. H., Reed, K. J., Guo, D. S., & Savin, D. W. 1998, Phys. Rev. A, 58, 4539
Cheng, K. T., Kim, Y.-K., & Desclaux, J. P. 1979, At. Data Nucl. Data Tables, 24, 111
Ferland, G. J., Korista, K. T., Verner, D. A., Ferguson, J. W., Kingdon, J. B., & Verner, E. M. 1998, PASP, 110, 761
Froese-Fischer, C. 1991, Comput. Phys. Commun., 64, 369
Gorczyca, T. W., Badnell, N. R., & Savin, D. W. 2002, Phys. Rev. A, 65, 062707
Grant, I. P., McKenzie, B. J., Norrington, P. H., Mayers, D. F., & Pyper, N. C. 1980, Comput. Phys. Commun., 21, 207
Gu, M. F. 2003a, ApJ, 579, L103
———. 2003b, ApJ, 582, 1241
Heerlein, C., Zwicknagel, G., & Toepffer, C. 2002, Phys. Rev. Lett., 89, 083202
Hess, C. J., Kahn, S. M., & Paerels, F. B. S. 1997, ApJ, 478, 94
Jacobs, V. L., Davis, J., Kepple, P. C., & Blaha, M. 1977, ApJ, 211, 605
Kallman, T. R., & Bautista, M. 2001, ApJS, 133, 221
Kilgus, G., Habs, D., Schwalm, D., Wolf, A., Badnell, N. R., & Müller, A. 1992, Phys. Rev. A, 46, 5730
Lampert, A., Wolf, A., Habs, D., Kilgus, G., Schwalm, D., Pindzola, M. S., & Badnell, N. R. 1996, Phys. Rev. A, 53, 1413
Mohamed, T., Nikolić, D., Lindroth, E., Madzunkov, S., Fogle, M., Tokman, M., & Schuch, R. 2002, Phys. Rev. A, 66, 022719
Müller, A., & Wolf, A. 1997, in Accelerator-Based Atomic Physics Techniques and Applications, ed. S. M. Shafroth & J. C. Austin (New York: AIP), 147
Ramadan, H. H., & Hahn, Y. 1989, Phys. Rev. A, 39, 3350
Roszman, L. J. 1987, Phys. Rev. A, 35, 3368
Savin, D. W., et al. 1997, ApJ, 489, L115
———. 1999, ApJS, 123, 687
———. 2000, in Proc. 12th APS Topical Conference on Atomic Processes in Plasmas, Reno Nevada, ed. R. C. Mancini (New York: AIP), 267
———. 2002a, ApJ, 576, 1098
———. 2002b, ApJS, 138, 337
Schippers, S., Müller, A., Gwinner, G., Linkemann, J., Saghiri, A. A., & Wolf, A. 2001, ApJ, 555, 1027
Schippers, S., et al. 2000, Phys. Rev. A, 62, 022708
Seaton, M. J., & Storey, P. J. 1976, in Atomic Processes and Applications, ed. P. G. Burke & B. L. Moisewitch (Amsterdam: North-Holland), 133
Shull, J. M., & van Steenberg, M. 1982, ApJS, 48, 95 (erratum 49, 351)
Tokman, M., et al. 2002, Phys. Rev. A, 66, 012703